RSC Advances

ROYAL SOCIETY OF CHEMISTRY

www.rsc.org/advances

Graphical abstract for:

Water soluble fluorophore-carbazole-Au-DNA nanohybrid: enhanced two-photon absorption for living cell imaging application

Shu-juan Zhu, Lin Kong, Hui Wang, Yu-peng Tian, Sheng-li Li, Zhao-ming Xue, Xian-yun Xu, and Jia-xiang Yang

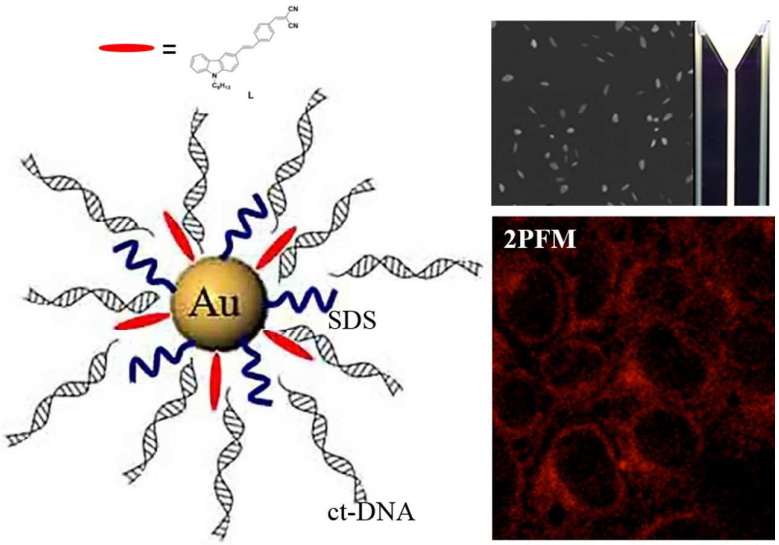

Water soluble **L**-Au-DNA nanohybrid exhibits enhanced 2PA properties which can widely and evenly uptake lysosome part of the HepG2 cells.

RSC Advances

RSCPublishing

ARTICLE

Water soluble fluorophore-carbazole-Au-DNA nanohybrid: enhanced two-photon absorption for living cell imaging application

Cite this: DOI: 10.1039/x0xx00000x

Received ooth April 2015,
Accepted ooth April 2015

DOI: 10.1039/x0xx00000x

www.rsc.org/

Shu-juan Zhu,[a] Lin Kong,*[a,b] Hui Wang,[a] Yu-peng Tian,[a] Sheng-li Li,[a] Zhao-ming Xue,[a] Xian-yun Xu[a], and Jia-xiang Yang*[a]

A type of water soluble Au based nanohybrid is constructed through a D-π-A (D=donor, A=acceptor) flurophore-carbazole derivative (abbreviated as **L**) coupled with gold nanoparticles (NPs) under the guidance of calf thymus DNA (ct-DNA). The coupling interactions between components at the interface increase the strength of donor-acceptor within the nanohybrid, which results in an energy transfer process and further brings about a dramatically blue-shift of single-photon absorption (about 53 nm from 450 nm for **L** to 397 nm for the hybrid) and fluorescence (~77 nm blue-shifted), decreased FL lifetime (1.65 ns for **L,** 0.53 ns for the hybrid), and blue-shift of two-photon excited fluorescence (2PEF, 638 nm for **L**, 574 nm for the hybrid). The couple effect amongst the nanohybrid also leads to enhancement of nonlinear optical properties, including two-photon absorption (TPA) cross section (δ, 137.60 GM for **L**, 651.07 GM for the hybrid) and two-photon absorption coefficient (β, from 0.003669 cm/GW to 0.01401). The two-photon fluorescence and good water solubility of the hybrid are proven to be potentially useful for two-photon microscopy imaging in living cells, such as HepG2.

1. Introduction

In the past few years, the nonlinear optical response (NLO) of colloids containing metallic nanoparticles (such as Au, Ag, Cu) have been investigated [1] for its promising applications in biological fields, such as bio-target sensing [2], two-photon excited fluorescence microscopy, high-resolution three-dimensional imaging of biological systems and optical limiting [3]. The previous investigations revealed that the surface plasmon resonance (SPR), occurred at the interface between the metal and the organic matrices, was the main driving force for the large NLO response, which also led to the synergy enhanced effect between the metallic nanoparticles and organic components. Thus, it is possible in principle, that modifying some parameters in a controllable way, such as various sizes and morphologies of nanoparticles, the structure selection of the organic matrices used to prepare the metallic nanomaterials, the preparation technique, and so on, would tailor the NLO response of the material to comply with the requirements of a specific application.

To choose an appropriate organic matrices, deoxyribonucleic acid (DNA) is one of the common-used biopolymer templates to construct metallic nanomaterials. For example, single-strand and/or double-helical DNA molecules can directly interact with metal ions, which can be used to reversibly assemble the creation of artificial metallic nanomaterials, such as gold [4], silver [5], palladium [6], platinum [7] and/or copper [8]. The multitudinous types and/or the usage variance of DNA can lead to different morphology or size of the metallic nanostructures, which can further lead to various functions, optical properties included. However, in order to obtain excellent second-order and/or third-order NLO properties, the size of this type of DNA-metal nanohybrid should be much small, which may lead to the difficulty in the preparation procedure. To simplify the preparation way, introducing another organic component with NLO functions will be an effective method [9]. To the best of our knowledge, the construction of this type of ternary hybrid NLO materials has rarely been reported yet, not to say change or enhance the NOL properties.

Herein, we have designed a bioprocessing material that can perform alterable linear/nonlinear optical functions with a single hybrid system, derived from an organic NLO component (**L** in this study) with a simple gold nanoparticle under the guidelines of ct-DNA [10]. The alterable and enhanced linear/nonlinear optical properties originated from the interactions between organic molecule, Au nanoparticle and ct-DNA at the interface, which was used to the application in two photon live-cell imaging.

2. Experimental

All chemicals are of analytical grade, purchased from Shanghai Chemical Reagent Company, solvents are purified using conventional methods before use.

2.1 Preparation of L

The preparation procedure of **L** was using our previous method [11] as described in **Scheme 1**. The detailed synthesis procedures of the intermediates ***a-c*** were provided in †ESI. To obtain **L**,

intermediate ***c*** (0.34 g, 1 mmol), Na_2CO_3 (0.11 g, 1 mmol), and dicyanomethane (0.20 g，3.0 mmol) were dissolved in 100 mL of ethanol, refluxed under N_2 atmosphere with TLC monitoring. After the completion of the synthesis, the reaction mixture was extracted with 500 mL of CH_2Cl_2 and the organic layer was washed three times with distilled water, and then dried with anhydrous magnesium sulphate overnight. The solvent was removed with a rotary evaporator. The residue was purified by column chromatography on silica gel with petroleum ether/ethyl acetate (50:1) as eluent to give 0.31 g (yield 81 %) target compound **L** as red powder. ^{1}H NMR (400 MHz, DMSO-d_6): δ (ppm) 8.46 (d, 2H, J = 4.0 Hz); 8.15 (d, 1H, J = 7.8 Hz); 8.00 (d, 2H, J = 8.4 Hz); 7.85 (d, 2H, J = 8.4 Hz); 7.80 (d, 1H, J = 8.8 Hz); 7.72 (d, 1H, J = 16.4 Hz); 7.63 (t, 2H, J = 8.8 Hz); 7.48 (t, 1H, J = 7.6 Hz); 7.40 (d, 1H, J = 16.4 Hz); 7.24 (t, 1H, J = 7.6 Hz); 4.41 (m, 2H (CH_2)); 1.78 (m, 2H (CH_2)); 1.24 (m, 6H (CH_2)); 0.81 (m, 3H (CH_3)). FT-IR (KBr cm^{-1}): 2922 (m), 2206 (C≡N, m), 1621 (m), 1561 (s), 1460 (s), 1389, 1208 (s), 754 (m).

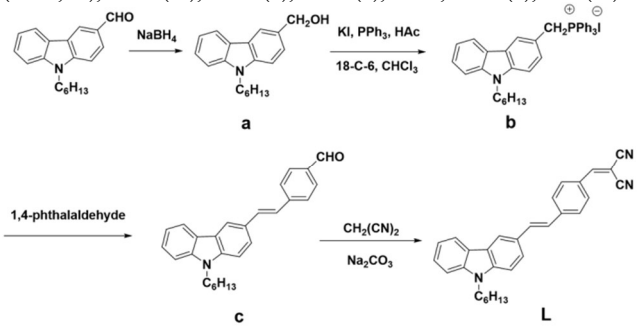

Scheme 1. The synthesis route of compound **L**

2.2 Preparation of L-Au-DNA nanohybrid

The hybrid materials were produced using a modified polyol process as our previous report [12]. Ethylene glycol (EG) was chosen as the solvent as it can reduce gold ion in high temperature [13]. To increase the solubility of the material in water and/or cell media, cysteine, a biological material in the body, was introduced into the hybridation process. For preparation of **L**-Au-DNA nanohybrid, **L** (16.3 mg, 0.05 mmol), ct-DNA (12.0 mg, 0.1 mmol), sodium dodecyl sulfate (SDS, 40 mg) were dissolved in 10 mL of EG, then $HAuCl_4$ (1 mL, 0.05 mol/L in EG solution) was added, followed by microwave heating for 2 min. During the process, the transparent solution changed from red to brown gradually. Then the solution was cooled to room temperature naturally and kept undisturbed overnight for precipitation. The precipitate was filtered and washed five times with excess high-purity water to remove excessive ct-DNA, SDS, EG and other inorganic residue, then dispersed into high-purity water (1.00 mg/mL) for structure characterization and optical property research.

Pure Au NCs and pure **L** nanostructures were prepared through the same process without ct-DNA and in the absence of **L** and $HAuCl_4$, respectively. For preparation of pure Au NCs, sodium dodecyl sulfate (SDS, 40 mg) and $HAuCl_4$ (1 mL, 0.05 mol/L) were dissolved in 10 mL of glycol (EG), the solution was then heated by microwave for 2 min. For preparation of pure **L** nanostructures, sodium dodecyl sulfate (SDS, 40 mg) and **L** (16.3 mg, 0.05 mmol) were dissolved in 10 mL of glycol (EG), then followed by microwave heating for 2 min.

2.3 Nonlinear optical measurements

The nonlinear optical properties of **L** nanostructrue and **L**-Au-DNA nanohybrid were measured through Z-scan measurement and two-photo-excited fluorescence (2PEF) with a concentration of 1.0×10^{-4} mol/L (based on Mol. Wt. of **L**) using femtosecond laser pulse and Ti:95 sapphire system (10 Hz, 140 fs). For 2PEF measurements, quartz-glass sample with 1.0 cm thickness were used. While for Z-scan measurements, the quartz-glass cell was 1.0 mm thick, and the average laser power was 36 mW. The optical path length for Z-scan was 5.0 cm from the sample. The excited wavelength was between 680 nm and 980 nm.

Nonlinear absorption coefficient β was measured by open aperture Z-scan technique. For the open aperture, the normalized transmittance as a function of the position along the z axis can be written as **equation 1**

$$Tz = \sum_{m=0}^{\infty} \frac{[-q(z)]^m}{(m+1)^{3/2}}, \text{ where } q(z) = \frac{\beta I_0 L_{eff}}{[1+(z/z_0)^2]\alpha} \qquad (1),$$

where Z_0 was the diffraction length of the beam, I_0 was the intensity of the light at focus, L_{eff} was the effective length of the sample, α was the linear absorption coefficient at the wavelength used.

Further, the molecular 2PA cross-section (δ) could also be determined through Z-scan measurement by using the following relationship, **equation 2**,

$$\delta = h\upsilon\beta \times 10^{-3}/N_A d, \qquad (2),$$

where h was the Planck's constant, υ was the frequency of input intensity, N_A was the Avogadro constant, and d was the concentration of the sample.

2.4 Cell culture, incubation and 2PFM imaging

In this study, HepG2 cells (human liver cancer cell) were chosen as the testing candidates, and were cultured and stained with the nanohybrid. HepG2 cells were seeded in 6 well plates at a density of 2×10^5 cells per well and grown for 96 hours. For live cell imaging, cell cultures were incubated with the chromophores (10% PBS: 90% cell media, PBS = phosphate buffered saline) at a concentration of 20 μM and maintained at 37 ºC in an atmosphere of 5% CO_2 and 95% air for incubation times ranging up to 30 min. The cells were then washed with PBS (3 × 3 mL per well). The cells were imaged using confocal laser scanning microscopy and water immersion lenses. All of the experiments were repeated three times. The measured data for each set of experiments were expressed with the average value.

HepG2 cells were fluorescence imaged on a Zeiss LSM 710 META upright confocal laser scanning microscope using 40 × magnification water-dipping lenses for the monolayer cultures. Image data acquisition and processing was performed using Zeiss LSM Image Browser, Zeiss LSM Image Expert and Image J.

2.5 Instruments

The morphologies were obtained on field-emission scanning electron microscope (FESEM, Hitachi S-4800) and electron microscope (TEM, JEM-2100). The Raman spectra were recorded with a Labram-HR spectrometer by exciting with the 325 nm radiation line of a argon ion laser. UV-vis absorption spectra were obtained on a LKB Biochem (Shimadzu UV-265) in the wavelength range of 200-800 nm. Fluorescence spectra were measured at room temperature using a Hitachi F-7000 spectrometer. Fluorescence life time and fluorescent quantum yield measurements were carried out using an HORIBA FluoroMax-4P fluorescence spectrometer equipped with a time-correlated single-photon counting (TCSPC) card. A reconvolution fit of the decay profiles was made with F900 analysis software to get the lifetime value.

3. Results and discussion

3.1 Morphological characterization

The nanohybrid was prepared by heating the EG solution containing **L**, $HAuCl_4$ and ct-DNA. The whole **L**-Au-DNA nanohybrid showed

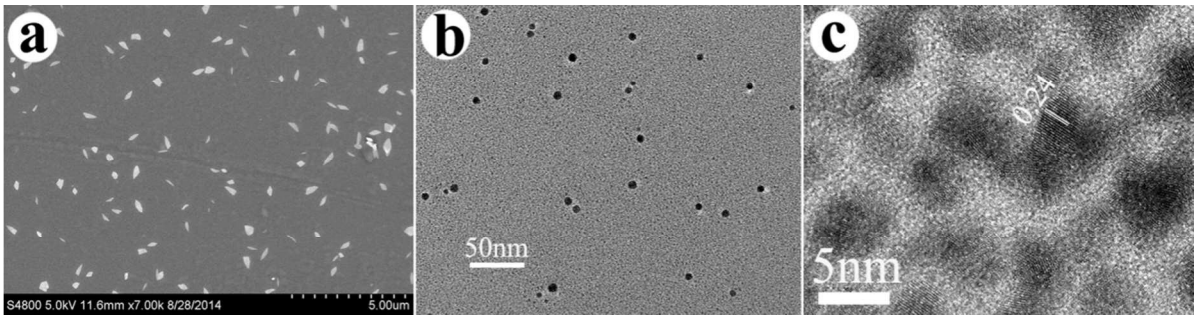

Figure 1 a) SEM image of **L**-Au-DNA nanohybrid, b) TEM and c) HRTEM image of Au NPs embedded in **L**-Au-DNA nanohybrid

flake-like structure with the size of about hundreds of nanometers (**Fig. 1a**), which was shorter and thinner than that of pure **L** nanostructures. Pure **L** nanostructures obtained from EG solution were shown in †ESI **Fig. S1**. Monodisperse 1-D belts of micro size were observed with lengths of about tens of micrometres and width of about 1~2 μm. The results indicated dramatically morphological change during this hybrid process. The somewhat strong interactions between Au NPs and organic components may responsible for the morphology changing.

Detailed investigation of the nanohybrid revealed that Au NPs were deeply buried in organic matrix. From TEM image (**Fig. 1b-c**), the morphology of Au NPs can be clearly observed. The Au NPs exhibited single crystalline structure with diameter of ~5 nm, which was smaller than the ~40 nm pure Au NPs prepared without **L**, as shown in †ESI **Fig. S5**. The results meant that the hybridization effect also affected the formation of Au NPs. The distinct lattice spacing was *ca.* 0.24 nm that was shown in **Fig. 1c**, corresponding well to the (111) plane of FCC Au NPs [14].

During the coupling process, Au^{3+} may interact with organic components when they were mixed at the very beginning. In hot EG solution during MW heating, Au^{3+} ions can be slowly reduced and tiny Au NPs with minor size and high surface energy were formed. Except for SDS and ct-DNA, **L** served as an important shape directing agent to guide the subsequent growth of the Au NPs as discussed previously. In hot EG solution, **L** and DNA were dissolved and tiny Au NPs were dispersed uniformly. When the solution was cooled naturally, some of **L** molecules were precipitated and drove Au NPs to precipitate along with them. Thus, Au NPs were wrapped in the organic matrix as a result. Then, the weak intermolecular interactions between adjacent **L** molecules, and the interactions between **L**, ct-DNA and Au ions at the interface may serve as the main driving force for the self-assembly process, which can lead the whole hybrid to form flake-like structure.

Detailed study revealed that the existence of ct-DNA was very important for the formation of flake-like **L**-Au-DNA nanohybrids. The control experiment showed that when ct-DNA was not used in the procedure, the morphology of the hybrid and the size of Au nanoparticles were absolutely different. As for **L**-Au hybrid, some nanobelts with the length was ~5 μm and the width was ~100 nm were captured as shown in †ESI **Fig. S4**, which aggregated together forming leaf-like dendrite structure. The Au nanoparticles were also embedded in the organic matrix, the size of which was about 40 nm and larger that of **L**-Au-DNA hybrid as discussed previously.

3.2 Linear Optical Properties

From the results and discussions mentioned above, the somewhat strong interactions between oragnic/inorganic components of the nanohybrid brought about significant changes of the morphology. Furthermore, the effect of the interactions on the linear optical properties was investigated. The results revealed an obvious increased and blue-shifted emission with the appearance of a new emission band and decreased FL lifetime.

3.2.1 UV-vis absorption

The UV-vis absorption spectrum of pure **L** nanoblets showed the molar extinction coefficient being 7.2 × 10^3 L·mol^{-1}·cm^{-1} exhibited three major absorption peaks at 291 nm, 345 nm and 450 nm (**Fig. 2a**), respectively. The latter corresponded to the π-π* transition of the whole π-conjugated **L** molecule, while the former two resulted from the transition of the small π-conjugated group, such as carbazole group [14]. The surface plasmon resonance (SPR) band of pure Au NPs centered at 501 nm with a shoulder band at 598 nm (**Fig. 2a**) with the molar extinction coefficient being 2.6 × 10^3 L·mol^{-1}·cm^{-1}. After the hybridation, the intrinsic transition centered at 291 nm showed

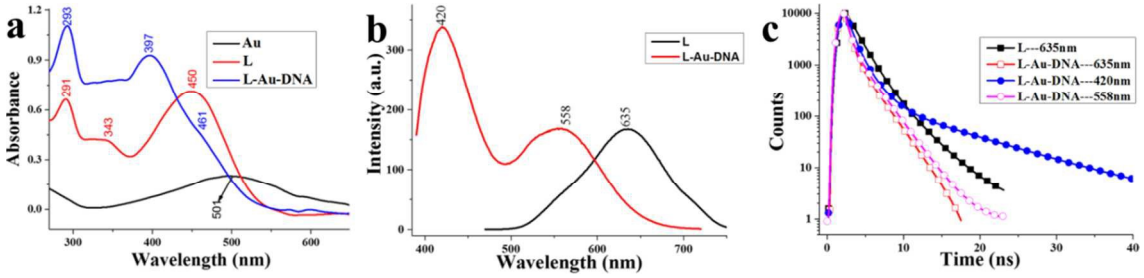

Figure 2 (a) UV-vis absorption spectra of pure **L** nanobelts (1.0 × 10^{-4} mol/L), pure Au NPs (8.0 × 10^{-5} mol/L) and **L**-Au-DNA nanohybrids (1.0 × 10^{-3} mol/L), respectively; (b) fluorescence spectra of pure **L** nanobelts and **L**-Au-DNA nanohybrids (1.0 × 10^{-4} mol/L for each); (c) time-domain fluorescence intensity decay of **L** detected at 635 nm, **L**-Au-DNA nanohybrids detected at 635 nm, 420 nm and 558 nm, respectively.

a slightly red-shift to 293 nm. While the π-π* transition of the whole π-conjugated **L** molecule centered at 450 nm red-shifted for 11 nm to 461 nm as a shoulder band. At the same time, it can also be observed that that there existed three new absorbance bands centered at 397 nm, 568 nm and 598 nm, respectively. The weak absorption band located at 568 nm and 598 nm can be regarded as coming from Au NPs. The molar extinction coefficient of the band located at 397 nm was lowered to be 9.3×10^2 L·mol^{-1}·cm^{-1}.

The results indicated that the main π-conjugated chain and the small π-conjugated fragment of **L** molecule were influenced during the hybridization procedure, which further revealed the strong interactions between components during the formation of the nanohybrid. As **L** is a D-π-A (D = donor, A = acceptor) type molecule endowing **L** with intramolecular charge transfer (ICT) feature. The interactions between **L**, ct-DNA molecules and Au ions at the surface of Au NPs can influence the ICT process, then slightly change the π-conjugated degree of **L** molecule, and affect the carbazole group as well. Thus, the appearance of the absorbance band centered at 397 nm can be regarded as the intrinsic absorbance coming for the new absorbing group formed at the interface. Here, ct-DNA played a vital role for the generation of new absorption band. The absorption bands for **L**-Au hybrid prepared without ct-DNA centered at 436 nm, 331 nm and 293 nm, respectively, as shown in †ESI Fig.S6a. The main π-π* transition of the whole **L** molecule showed a simple blue-shift for about 14 nm, while the transition of small π-conjugated group showed a blue-shift for about 12 nm. There also existed a small band at 556 nm, which can be regarded as coming from aggregated Au NPs. The most obvious was that there did not appear the band at 397 nm. The phenomenon clearly revealed the absorption at 397 nm was the intrinsic transition of **L**-Au-DNA nanohybrid, which also indicated the important role of ct-DNA on the optical property except for the guiding role in synthesis process of water soluble Au nanoparticles.

3.2.2 Fluorescence emission

Furthermore, the emission profile of the nanohybrid also differed significantly with that of pure **L** nanobelts, both in terms of intensity and wavelength. The **L** nanobelts emitted red light under illumination with a 365 nm UV lamp (insert in †ESI **Fig. S7a**), the emission band of which centered at 635 nm (**Fig. 2b**). The emission of pure Au NPs was not detected in this study.

After hybridation process, the nanohybrid displayed a broad, white emission profile with two emission band entered at 558 nm and 420 nm, respectively. The white light can be seen clearly under illumination with a 365 nm UV lamp which was shown in **Fig. S7b**. The emission band at 558 nm appeared as a shoulder band and showed an obvious blue-shift for about 120 nm from that of pure **L** nanobelts. The luminescence intensity of the main emission band at 420 nm was enhanced by 3 times with respect to that of pure **L** nanobelts.

There are two mechanisms to explain the enhanced emission. The one is that metal enhanced fluorescence (MEF) [15] may lead the phenomenon, which also revealed that the distance between **L** component and Au NPs at the interface was larger than 50 Å [16].

The other is that the enhancement emission intensity could be due to the generation of low concentration of **L** molecules as a result of the existence of embedded Au NPs, which was concluded from the phenomenon that **L** exhibited traditional ACQ (aggregation-caused quenching) properties as shown in †ESI Fig. S8. In the structure of **L** molecule, carbazole group and dicyano unit were connected between ethylenic bond and benzene unit which caused an extended coplanar π-conjugated structure, strong π-π stacking effect was the main feature between the adjacent molecules, whereby the emission in the aggregates can be quenched. As for **L**, benzene was a good solvent and ethanol was a bad solvent. Adding ethanol to a benzene solution of **L** will cause the well-dissolved molecules to aggregate, which resulted in quenching of the emission. For compound **L**, the concentration was kept at 1.0×10^{-4} mol•L^{-1}. As shown in †ESI Fig. S8, **L** showed a dramatic change of fluorescence intensity from the weak isolated single molecule in benzene solution to the weakly fluorescent nanoparticles suspension in benzene-ethanol solution. An obvious quenching was observed when the volume ratio of ethanol to benzene was over 1:9, which could be related to the aggregate formation. The fluorescence intensity of **L** in the aggregate state was apparently weaker than that of the pure benzene solution. A similar phenomenon will appear before and after the hybridization process. The π-π interactions between adjacent **L** molecules in **L** nanoblets brought about weak emission due to the as-discussed ACQ effect. While in the hybrid system, when Au NPs embedded in **L** matrixes, π-π interactions between **L** molecules was decreased or cut off in some points, which brought about decreasing of ACQ effect and resulted in fluorescence intensity enhancement of the whole nanohybrid.

To better understand the function of ct-DNA on the optical properties, the fluorescence emission of **L**-Au hybrid was also detected as shown in †ESI **Fig. S6b**. The main difference of fluorescence emission spectrum from that of **L**-Au-DNA was that the **L**-Au hybrid showed just one emission band which centered at 605 nm, which blue-shifted for about 30 nm from that of pure **L**. The results indicated that the existence of ct-DNA enlarged the ICT process of **L** to some more extent than that when only Au nanoparticles were introduced into the system.

3.2.3 Time-resolved fluorescence measurement

Further, the time-resolved photoluminescence measurements for **L** and **L**-Au-DNA hybrid were carried out. The fluorescence decay of **L** detected at 635 nm yielded an average FL lifetime of 1.65 ns and fitted with a double exponential components, which indicated that there existed two kinds of fluorescent components. The result was in accordance with the excitation bands of **L** (†ESI **Fig. S9**). A short component had a decay lifetime of 1.50 ns (the corresponding amplitude A = 91%), and the following component had 3.25 ns (9%).

In contrast, the fluorescence lifetime for **L**-Au-DNA hybrid detected at 558 nm was found to be 0.53 ns. When it was detected at 420 nm, the fluorescence lifetime was 1.11 ns. This decay study clearly demonstrated that **L**-Au-DNA hybrid exhibited lower FL lifetime compared to pure **L**. Furthermore, the fluorescence of the **L**-Au-DNA hybrid was decayed with three components. For example, when **L**-Au-DNA hybrid was detected at 558 nm, the corresponding amplitude (A) of a long component was 2.13 ns with A = 9%, followed by a short component with τ = 0.65 ns and A = 29%. At the same time, a new component appeared with a short lifetime being 0.23 ns and the amplitude as 62%, respectively. The results confirmed the existence of a new fluorophore system in the **L**-Au-DNA nanohybrid, an observation that was attributed to tiny Au NPs in close proximity to **L** molecules, as discussed previously.

Table 1 Fluorescence decay lifetime (τ) and amplitude (A) of fluorescence of **L** and **L**-Au-DNA nanohybrid

	λ (nm)	τ1(ns)	A1(%)	τ2(ns)	A2(%)	τ3(ns)	A3(%)	$\bar{\tau}$ (ns)	χ^2	ϕ_{ET}(%)
L	635	1.50	91	3.25	9	-	-	1.65	1.23	
L-Au-DNA	635	0.29	45	0.59	46	2.08	9	0.59	1.01	64.2
	558	0.23	62	0.65	29	2.13	9	0.53	1.03	
	420	0.77	74	1.71	25	9.65	1	1.11	1.01	

It is known that an increase in the radiative rate will decrease the lifetime. In this study, the third component with a shorter lifetime revealed the presence of an additional fast nonradiative decay channel. It is known that the FL lifetime of fluorophores is inversely proportional to the sum of the radiative decay rate (k_{rad}^0) and the nonradiative decay rate (k_{nr}^0) [17]. When Au NPsare in close contact with the fluorophores (**L** in this study), they can affect the intrinsic radiative and/or nonradiative decay rate of the fluorophores. In this study, enhanced emission of **L**-Au- DNA may bring about prolonged FL lifetime, belonging to the radiative decay rate. Thus, the decreased FL lifetime of **L**-Au-DNA nanohybrids revealed that the existence of Au NPs affected the nonradiative decay rate to a much more extent. From what has been discussed above, the plasmon-exciton interaction between the components was responsible for the phenomenon, a fact that resulted in the energy-transfer process. The energy transfer efficiency (ϕ_{ET}) was estimated using **Equation (3)** [18].

$$\phi_{ET} = 1 - \frac{\tau_{\text{hybrid}}}{\tau_L} \quad (3),$$

where τ_{hybrid} was the average FL lifetime of **L** component in the **L**-Au-DNA nanohybrids detected at 635 nm, which was 0.59 ns as shown in Table 1. τ_L was the average lifetime of free **L** (1.65 ns as discussed above). From these data, the energy may transfer from **L** to Au NPs in the nanohybrid and the estimated energy transfer efficiency was calculated to be 64.2 %.

Here, the existence of ct-DNA enhanced the energy transfer efficiency. The fluorescence lifetime for **L**-Au hybrid prepared without ct-DNA detected at 605 nm was found to be 0.85 ns. When it was detected at 635 nm, the fluorescence lifetime was 0.72 ns. This decay study clearly demonstrated that **L**-Au hybrid exhibited lower FL lifetime compared to pure **L** and longer FL lifetime compared to that of **L**-Au-DNA hybrid. The corresponding energy transfer efficiency of amongst the components of **L**-Au hybrid was calculated to be 56.4% (†ESI **Table S1**), which was lower than that of **L**-Au-DNA. The results confirmed the important role of ct-DNA on the optical properties. Based on the results mentioned above, the formation process of the novel hybrid was presented in Fig. S4. L molecules can self-assemble into one-dimensional structures due to weak interactions between neighboring molecules. When $AgNO_3$ is introduced during the aggregation process, the assembly of L and the formation of Ag NCs occur simultaneously and affect each other. Lastly, nanohybrids consisting of Ag NCs uniformly dispersed on L nanoribbons appear.

3.3 Electrochemical Property

The energy transfer effect between the components described above revealed the energy level matching between them. To further study the coupling effect, the energy gap and energy transfer between the components, **L** had been analyzed by cyclic voltammetry in the presence of Bu_4NClO_4 (TBAP, 0.1 M) as supporting electrolyte with a scan rate of 50 $mV \cdot S^{-1}$ using a reference Ag/AgCl electrode [19]. Due to the presence of strong electron donor moieties and dicyano unit in **L**, in CV experiments they displayed complex redox behavior involving multistep oxidation processes as shown in **Fig. 3a**. The first onset oxidation potential of **L** was 1.06 V, which can be identified as the oxidation of carbazole unit (†ESI **Fig. S11**). The estimated HOMO level in vacuum was -5.44 eV (E_{HOMO} = -e(E_{onset} + 4.38) eV), which was in agreement well with the results from the theoretical calculation, and the HOMO level was also close to the Femi level of Au (-5.10 eV).

A HOMO-LUMO gap of 2.27 eV of **L** was estimated from the absorption edge ((edge = 546 nm obtained from **Fig. 2a**). The results

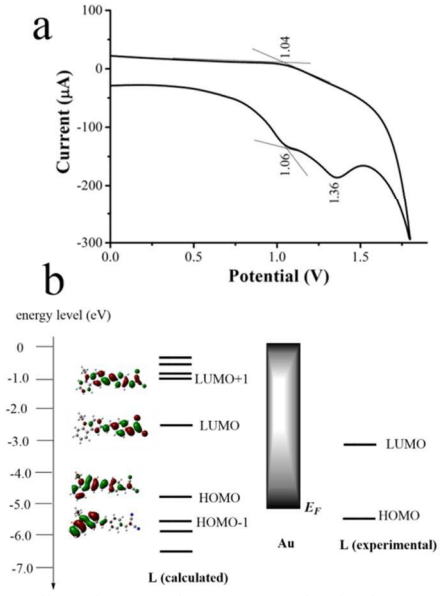

Figure 3 (a) Cyclic-voltammetric response of **L** in the presence of 0.1 M TBAP *Vs.* Ag/AgCl at room temperature. Scan rate: 50 mV/s; (b) Calculated frontier orbital and the corresponding energy of **L** in the gas phase and electronic energy level alignments for Au and **L** (both from calculated and experimental data).

from the theoretical calculation, and the HOMO level was also close to the Femi level of Au (-5.1 eV). LUMO energy level was calculated to be -3.17 eV by subtraction of the optical band gap from the HOMO energy levels ($E_{LUMO} = E_{HOMO} + E_{opt}$).

The second oxidation potential of **L** was 1.36 V, which can be identified as the oxidation of the cyano group. The two oxidation potentials were higher than that of Au^{3+}/Au electrode (0.72 V as shown in †ESI **Fig. S12**). Thus, oxidation-reduction reaction won't occur between **L** and Au^{3+} in the reaction mixture, which may be responsible for the stability of **L** in DNA-$HAuCl_4$-EG solution and the corresponding nanohybrids. The electronic levels of **L** and the relative position of the Femi level of Au from experimental results were depicted in **Fig. 3b**.

Furthermore, the time-dependent density functional theory (TD-DFT) was used to study the electron cloud distribution and energy level of the **L** molecule. The results also showed difference between the Femi level of Au and the HOMO-LUMO level of **L**. The calculated results were also listed in **Fig. 3b**. The LUMO level of **L** was calculated to be -2.62 eV. The HOMO-1 level of **L** was -5.34 eV, which was close to the Femi level of Au (-5.1 eV) and also close to the data calculated from the first onset oxidation potential. Thus, when **L** and Au were in close contact, the electron redistribution may come true and the change of optical properties may appear. The calculated results also revealed that the main transition for **L** (λ_{abs} = 460 nm) was just from the configuration HOMO-1 orbit to LUMO orbit with the oscillator strength $f_{(HOMO-1)-LUMO}$ being 0.6915.

3.4 Raman scattering experiment

As discussed above, the interactions between the organic and inorganic components in **L**-Au-DNA nanobybrid brought about significant changes of morphology and linear optical properties. To further investigate the interaction 'hot spot' at the interface, Raman and FT-IR spectral experiments were carried out. The 'hot spot' functional group can be determined by comparing relative intensities and frequency shifts of the Raman and/or FT-IR bands of **L** before and after the hybridization process. The Raman scattering spectra of **L** and the hybrid were given in **Fig. 4** and **Fig. S13**. The spectra clearly indicated that the Raman scattering of **L** in the **L**-Au-DNA hybrids was significantly enhanced as shown in **Fig. 4** and †ESI **Fig. S13**, compared to that of pure **L**, especially the bands centered at about 839, 892, 1059, 1087, 1294, 1434 and 1461 cm^{-1}. The surface enhanced Raman scattering (SERS) phenomenon may bring about the enhancement [20].

Moreover, several differences between the spectra can also be observed. The sharp bands at 1566 cm^{-1}, 1594 cm^{-1} and 1622 cm^{-1} in normal Raman spectrum of **L** were attributed to the ring breathing of the benzene ring, the C=C stretching vibration [21], respectively. After coupling with Au NPs in the assistance of ct-DNA, these three bands changed to a board band from 1566 cm^{-1} to 1615 cm^{-1} which centered at 1591 cm^{-1} with the FWHM (full width at half maximum) being 17 cm^{-1}. At the same time, the band at 1437 cm^{-1} down-shifted by 3 cm^{-1} to 1434 cm^{-1} with a shoulder band at 1461 cm^{-1}. Also, the FWHM (full width at half maximum) of this band broadened from 6 cm^{-1} to 45 cm^{-1} upon coupling. The band at 1325 cm^{-1} down-shifted by 31 cm^{-1} to 1294 cm^{-1}. There also existed some new bands centered at 1087 cm^{-1}, 1059 cm^{-1}, 892 cm^{-1} and 839 cm^{-1}, respectively. These new scattering bands and the shift of those mentioned

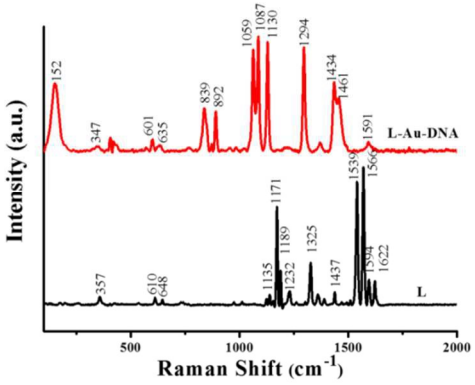

Figure 4 Raman spectra of **L** and **L**-Au-DNA nanohybrid

above indicated that the couple interactions between the components took place through the π-conjugated group.

Moreover, there also existed a new band centered at 152 cm^{-1}, which clearly revealed the formation of Au-N bond, which showed that the interactions also took place at the N atom of the **L** molecule. The FT-IR spectra (†ESI **Fig. S14**) showed that the transmittance band of cyano unit centered at 2224 cm^{-1} down-shifted to 2148 cm^{-1} when the hybrid confirmed. The results was indicated that the vibration of cyano unit became weak when **L** hybriding with Au NPs in the assistance of ct-DNA. Combing with the phenomenon that the Raman scattering band of cyano unit centered at 2225 cm^{-1} became very weak, it can be concluded that the interaction 'hot spot' may also took place at N atoms of cyano unit.

The results of Raman scattering and FT-IR analysis revealed intermolecular interactions between π-conjugated group, cyano unit and Au nanoparticles. The large enhancement factors may be due to the coupling of the localized surface Plasmon (LSP) of Au NPs and the enhanced electromagnetic field intensity localized at the interface. The weak interactions further influence the electronic distribution of **L**, which accounted for the changes observed in the SERS spectra and the linear optical properties.

3.5 Nonlinear optical properties

3.5.1 Two-photon excited fluorescence (2PEF)

Except for the appearance of the tuneable linear optical properties, the intermolecular interactions existed at the interface of the nanohybrid and the corresponding changeable ICT process also resulted in significant difference of 2PEF.

In linear absorption test, there was no linear absorption in the wavelength range of 550-900 nm for **L** and the nanohybrid, which inferred that there were no energy levels corresponding to one electron transition in this spectral range. Therefore, the 2PEF pathway was expected to appear if frequency up-converted fluorescence induced with a laser in this range appeared. †ESI **Fig. S15** showed log-log plot of the excited fluorescence signal *vs.* excited light power. The linear dependence of the square of input laser power on the output fluorescence intensity (with a slope of 2.30 and 2.02 for **L** and nanohybrid respectively) provided direct evidence for two-photon excited process (†ESI **Fig. S15**).

The best 2PA wavelength obtained from Z-scan experiments was 880 nm for **L** and 800 nm for **L**-Au-DNA. The 2PEF and Z-scan curve of pure Au NPs were not captured when it was excited between 680~980 nm in this study. The best excitation wavelength of **L** was slightly shorter than twice that of the corresponding linear

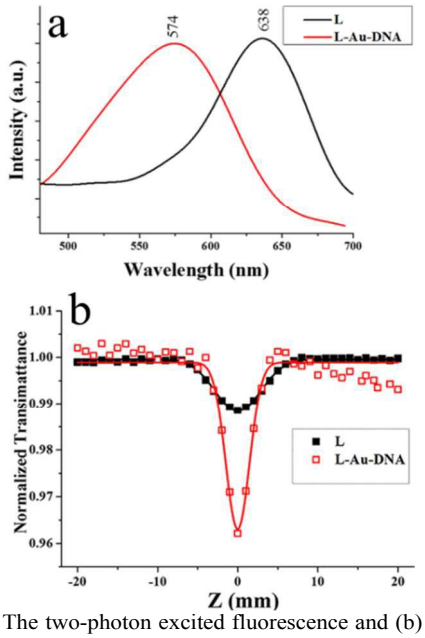

Figure 5 (a) The two-photon excited fluorescence and (b) open Z-scan experiments of **L** and **L**-Au-DNA nanohybrid, respectively. The concentration was 1.0×10^{-3} mol/L.

absorption maximum (450 nm) while the best excitation wavelength of **L**-Au-DNA was just nearby the twice of the corresponding linear absorption maximum (397 nm). The best 2PA wavelength being 800 nm for **L**-Au-DNA also revealed that the 2PA of it was mainly came from the **L** component.

The 2PEF spectra of the samples were shown in **Fig. 5a**, respectively. The 2PEF emission maxima located at 638 nm for **L**, which was very close to the fluorescence wavelength using one photon emission fluorescence (1PEF, 635 nm as shown in **Fig. 2b**). As for the 2PEF of **L**-Au-DNA hybrid, there existed only one main emission peak located at 574 nm, which was different from the two main emission peaks of 1PEF and showed a red-shift when compared to that of 1PEF (**Fig. 2**). However, the 2PEF intensity of **L**-Au-DNA exhibited a decrease compared to that of **L**, which was also different from the enhancement of 1PEF as well. The results indicated the difference of the excited states for 1PEF and 2PEF, mainly during the excitation process: two-photon absorption *vs* single-photon absorption [22].

There are two factors to influence the 2PEF intensity. One is that the interactions between organic molecules and Au NPs through the π-conjugated units, as discussed above, will enlarge the π-conjugated system which may increase the 2PEF intensity of the whole nanohybrid [23]. The other is the scattering phenomenon [24] that caused from the nanoparticles, which may result in quenched 2PEF, along with the heavy atom effect [25]. As for **L**-Au-DNA nanohybrid, the heavy atom effect and the scattering phenomenon may be the dominant factor of the decrease.

3.5.2 Open Z-scan experiment

Open aperture Z-scan experiments were carried out using femtosecond laser pulse to investigate nonlinear optical (NLO) properties of the samples, and the results were shown in **Fig. 5b**. The best input laser wavelength determined from Z-scan experiments was 880 nm for **L** and 710 nm for **L**-Au-DNA, respectively. All of the Z-scan curves displayed a decrease in transmittance at the focal point of the laser, which was typical of a positive NLO effect. The minimum transmittances at Z = 0 were 98.85 and 96.20% for the **L** and **L**-Au-DNA, respectively.

Based on the **Equation 1** (shown in Experimental Section), the 2PA coefficient β of **L** was calculated to be 0.003669 cm/GW, which was 0.01401 cm/GW for the nanohybrid. Slightly enlarged aggregate degree and strong electron coupling effects made significant contribution to the enhancement of the 2PA coefficient.

Based on **Equation 2**, the calculated 2PA cross section δ was 137.60 GM (1 GM = 10^{-50} cm^4 s/photon^{-1}) for **L**, which increased for about 5 times to 651.07 GM of the nanohybrid. The δ_{2PA} values of the samples were larger than that of many fluorophores widely used in biology, such as fluorescein and BODIPY [26], indicating the potential application, such as in 2PEF bioimaging.

Furthermore, based on the enhancement of 2PA coefficient β and 2PA cross section δ, it can be speculated that there are 3-5 **L** molecules in a **L**-Au-DNA unit [27]. Also, according to the solubility of the hybrid in water, it was reasonable that the ct-DNA fragments in the hybrid was more than **L** molecules. Thus, the possible molecular arrangement of a single **L**-Au-DNA hybrid unit was schematically demonstrated in **Fig. S10**.

3.6 Two-photon microscopy bioimaging application

As is known that the water solubility and biocompatibility of the material can influence the 2PEF bioimaging results. As for **L**-Au-DNA hybrid, the solubility of it in water was very good.

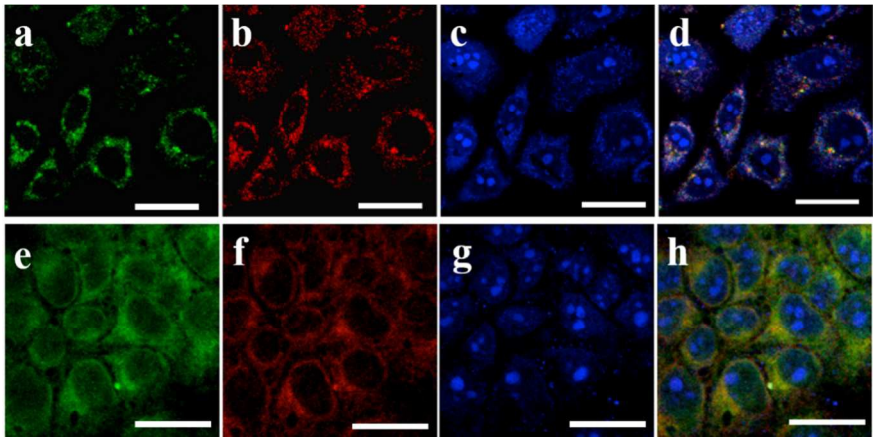

Figure 6 Spatial distributions of **L**, **L**-Au-DNA and Syto-Select in HepG2 cells. (a) one-photon image (λex = 450 nm), (b) two-photon image (λex = 880 nm) of HepG2 cells incubated with 10 μM of **L** (emission wavelength from 600 nm to 660 nm), after 2 hours of incubation, washed by PBS buffer. (e) one-photon image (λex = 420 nm), (f) two-photon image (λex = 800 nm) of HepG2 cells incubated with the **L**-Au-DNA nanohybrid (emission wavelength from 530 to 600 nm), after 1 hour of incubation, washed by PBS buffer. (c) and (g) Fluorescent images of HepG2 cells stained with Syto-Select for 10 min. (d) and (h) overlay images for a-c, and e-g, respectively. The scale bar was 20 μm.

To evaluate the performance of the as-prepared water soluble hybrid in live cells, a 2PFM imaging was conducted. HepG2 cells (human liver cancer cell) were the testing candidates,cultured and stained with the samples [28]. Two-photon excitation cell imaging using **L**, and the nanohybrid were achieved by using HepG2 cancer cells with a two-photon laser scanning confocal microscopy (**Fig. 6**). Treated cells were excited at proper 2PA wavelength, which was 880 nm for **L**, 800 nm for the nanohybrid, respectively.

The green channels in **Fig. 6a** and **6e** showed one-photon fluorescence microscopy (1PFM) images of **L** and **L**-Au- DNA nanohybrid, respectively. The red channel in **Fig. 6b** and **6f** showed 2PFM imaging of **L** and the nanohybrid, respectively. To determine precisely where the compounds were located [29], a standard fluorescence dye, Syto-Select that can stain nuclear and cytosolic RNA in living cells, was used as the secondary markers in this study. The blue channels in **Fig. 6c** and **6g** showed the fluorescent images of HepG2 cells stained with the Syto-Select.

The 1PFM and 2PFM imaging results showed in **Fig. 6** clearly revealed that both **L** and the nanohybrid successfully internalised with HepG2 cells. One-photon and two-photon induced fluorescence emissions were observed predominantly from the cellular cytoplasmic region. Both for **L** and the nanohybrid, the confocal micrograph showed endosomal and/or lysosomal like interaction. The luminescence that came from the lysosome implied that **L** and the nanohybrid permeated the phospholipid bilayers of cellular lysosome and bonded with lysosome leading to the eventual fluorescence [30]. The co-localization results listed in **Fig. 6c** and **6g** also confirmed the good cell viability after **L** and/or **L**-Au-DNA incubation.

Moreover, the 2PFM image showed that after one hour incubation with HepG2 cells under low concentration of **L**-Au-DNA (10 μM), the nanohybrid can widely and evenly uptake lysosome part all around the HepG2 cells. However, for **L**, as long as 2-4 hours incubation, only small parts of the lysosome were uptaken as shown in **Fig. 6a-b** and **S17**. Maybe the good solubility of the nanohybrid in water medium caused the phenomenon. When **L** was introduced into the cell, bad solubility of it resulted in less material entering and uneven distribution as shown in **Fig. 6a-b** and **S17**. On the contrary, after **L** coupled with Au NPs under the guidance of ct-DNA, the water solubility increased [31], which led the whole nanohybrid uniformly introduced into the cytoplasm. The results of the 1PFM and 2PFM imaging revealed that the water soluble nanohybrid were cell-permeable, suitable for cytosol staining, in live cells, and that the nanohybrid was clearly capable of indicating the lysosome section in HepG2 cells.

Conclusions

In this study, a water soluble Au-based nanohybrid with 2PA property was designed and prepared under the guideline of ct-DNA and flurophore-carbazole derivative (**L**). The existence of ct-DNA increased the water solubility of the nanohybrid. The exciton-plasmon interactions and the corresponding energy transfer process between the components brought about changeable linear optical property and enhanced nonlinear optical properties. The enhanced 2PA cross section and increased water solubility of the nanohybrid cause it suitable for cytosol staining in HepG2 cells, which exhibited high 2PEF sensitivity.

This study revealed that the simply preparation of Au-based nanohybrid under the guidance of organic 2PA molecule (**L**) and water soluble ct-DNA can increase the 2PA cross section and water solubility of the hybrid, which can decrease the difficulty of the preparation of the 2PA material for potential bio-imaging applications.

Acknowledgements

This work was supported by the Natural Science Foundation of Anhui Province (1508085SMB208), the NSFC (No: 51432001), and Educational Commission of Anhui Province of China (KJ2014ZD02).

Notes and references

[a]Department of Chemistry, Key Laboratory of Inorganic Materials Chemistry of Anhui Province, Anhui University, 111th Jiu-Long Road, Hefei, P.R. China.

[b]State Key Laboratory of Rare Earth Resources Utilization, Changchun Institute of Applied Chemistry, Chinese Academy of Sciences, 5625 Renmin Street, Changchun 130022, Jilin, PR China.

*Corresponding author. E-mail address: konglin_2009@126. com; jxyang@ahu.edu.cn.

† Electronic Supplementary Information (ESI) available: [SEM image of pure L nanostructure; TEM image of pure Au NPs; SEM and TEM images of **L**-Au-DNA nanohybrid; SEM image of L-Au nanohybrid prepared without ct-DNA. Chromaticity diagram (CIE) of fluorescence emission of the samples with photos of the materials under 365 nm UV light. Cyclic-voltammetric response of carbazole and $HAuCl_4$. Excitation spectrum of **L**. ACQ effect of **L**. The logarithmic plots of the output two-photon excited fluorescence *vs* the square of input laser of the samples. The photo of **L**-Au-DNA nanohybrid in water solution.]. See DOI: 10.1039/b000000x/

1 W. Sun, Y. Z. Zhu, A. R. Wang, L. Kong, S. L. Li, J. Y. Wu and Y. P. Tian, *New J. Chem.,* 2015, **39**, 6830; F. R. Udayabhaskar, B. Karthikeyan, P. Sreekanth and R. Philip, *RSC Adv.*, 2015, **5**, 13590.

2 K. Iliopoulos, D. Athanasiou, A. Meristoudi, N. Vainos, S. Pispas and S. Couris, *Phys. Stat. Sol. A*, 2008, **205**, 2635.

3 M. L. Liu, Q. Tang, T. Deng, H. J. Yan, J. S. Li, Y. H. Li and R. H. Yang, *Analyst*, 2014, **139**, 6185.

4 J. S. Sun, X. L. Wang, J. F. Liu, P. B. Wan, Q. Liao, F. Wang, L. Luo and X. M. Sun, *RSC Adv.*, 2014, **4**, 35263; A. K. Singh, D. Senapati, S. G. Wang, J. Griffin, A. Neely, P. Candice, K. M. Naylor, B. Varisli, J. R. Kalluri and P. C. Ray, *ACS Nano*, 2009, **3**, 1906; W. L. Chen, F. C. Lin, Y. Y. Lee, F. C. Li, Y. M. Chang and J. S. Huang, *ACS Nano*, 2014, **8**, 9053.

5 X. Lan, X. X. Lu, C. Q. Shen, Y. Y. Ke, W. H. Ni, and Q. B. Wang, *J. Am. Chem. Soc.*, 2015, **137**, 457; Z. T. Li, Z. N. Zhu, W. J. Liu, Y. L. Zhou, B. Han, Y. Gao, and Z. Y. Tang, *J. Am. Chem. Soc.*, 2012, **134**, 3322; W. Wang, N. Zhao, X. X. Li, J. Wan and X. L. Luo, *Analyst*, 2015,**140**, 1672.

6 C. I. Richards, S. Choi, J. C. Hsiang, Y. Antoku, T. Vosch, A. Bongiorno, Y. L. Tzeng and R. M. Dickson, *J. Am. Chem. Soc.*, 2008, **130**, 5038; T. Li, L. B. Zhang, J. Ai, S. J. Dong, and E. K. Wang, *ACS Nano*, 2011, **5**, 6334; L. B. Zhang, J. B. Zhu, S. J. Guo, T. Li, J. Li, and E. K. Wang, *J. Am. Chem. Soc.*, 2013, **135**, 2403.

7 Y. Hatakeyama, M. Umetsu, S. Ohara, F. Kawadai, S. Takami, T. Naka and T. Adschiri, *Adv. Mater.*, 2008, **20**, 1122.

8 M. Z. Li, Y. X. Pan, X. Y. Guo, Y. H. Liang, Y. P. Wu, Y. Wen and H. F. Yang, *J. Mater. Chem. A*, 2015, **3**, 10353; K. V. Nguyen and S. D. Minteer, *Chem. Commun.*, 2015, **51**, 4782.

9 Q. Wang, Q. Wang, M. Li, S. Szunerits and R. Boukherroub, *RSC Adv.*, 2015, **5**, 15861; Z. H. Li, S. Guo and C. Lu, *Analyst*, 2015, **140**, 2719.

10 T. Lee, A. K. Yagati, J. H. Min and J. W. Choi, *Adv. Funct. Mater.*, 2014, **24**, 1781.

11 L. Kong, J. X. Yang, Z. M. Xue, H. P. Zhou, L. J. Cheng, Q. Zhang, J. Y. Wu, B. J. Jin, S. Y. Zhang and Y. P. Tian, *J. Mater. Chem. C*, 2013, **1**, 5047.

12 L. Kong, J. X. Yang, Qi. Y. Chen, Q. Zhang, W. D. Ke, Z. M. Xue, H. P. Zhou, J. Y. Wu, B. K. Jin, and Y. P. Tian, *J. Nanopart. Res.*, 2014, **16**, 2324.

13 J. Kou, C. Bennett-Stamper and R. S. Varma, *ACS Sustainable Chem. Eng*., 2013, **1**, 810.

14 J. Yang, H. I. Elim, Q. B. Zhang, J. Y. Lee, and W. Ji, Rational synthesis, self-assembly, and optical properties of PbS-Au heterogeneous nanostructures via preferential deposition. *J. Am. Chem. Soc.*, 2006, **128**, 11921.

15 Y. H. Gao, J. Y. Wu, Q. Zhao, L. X. Zheng, H. P. Zhou, S. Y. Zhang, J. X. Yang and Y. P. Tian, *New J. Chem.*, 2009, **33**, 607; Z. H. Zeng, S. Mizukami, K. Fujita and K. Kikuchi, *Chem. Sci.*, 2015, **6**, 4934.

16 L. Kong, J. X. Yang, X. P. Hao, H. P. Zhou, J. Y. Wu, F. Y. Hao, L. Li, S. Y. Zhang, B. K. Jin, X. T. Tao, M. H. Jiang and Y. P. Tian, *J. Mater. Chem.*, 2010, **20**, 7372.

17 K. S. Kim, J. H. Kim, H. Kim, F. Laquai, E. Arifin, J. K. Lee, S. I. Yoo, B. H. Sohn, *ACS Nano*, 2012, **6**, 5051.

18 A. Panáček, L. Kvítek, R. Prucek, M. Kolář, R. Večeřová , N. Pizúrová, V. K. Sharma, T. Nevěčná, R. Zbořil, *J. Phys. Chem. B* 2006, **110**, 16248; T. L. Jennings, M. P. Singh, G. F. Strouse, *J. Am. Chem. Soc.*, 2006, **128**, 5462.

19 M. Choudhary, S. Siwal and K. Mallick, *RSC Adv.*, 2015, **5**, 58625.

20 D. Swiech, Y. Ozaki, Y. Kim and E. Proniewicz, *Phys. Chem. Chem. Phys.*, 2015, DOI: 10.1039/C5CP90117K; P. Zheng, M. Li, R.Jurevic, S. K. Cushing, Y. X. Liu and N. Q. Wu, *Nanoscale*, 2015, **7**, 11005; X. Gong, J. Tang, Y. X. Ji, B. B. Wu, H. P. Wu and A. P. Liu, *RSC Adv.*, 2015, **5**, 42653.

21 S. M. Morton and L. Jensen, *J. Am. Chem. Soc.* 2009, **131**, 4090.

22 P. Milosz, A. C. Hazel, G. D. Robert and L. A. Harry, *Angew. Chem., Int. Ed.*, 2009, **48**, 3244.

23 L. Li, Y. P. Tian, J. X. Yang, P. P. Sun, L. Kong, J. Y. Wu, H. P. Zhou, S. Y. Zhang, B. K. Jin, X. T. Tao and M. H. Jiang, *Chem. Commun.*, 2010, **46**, 1673.

24 M. Retsch, M. Schmelzeisen, H. J. Butt and E. L. Thomas, *Nano Lett.*, 2011, **11**, 1389.

25 M. Mac, A. Danel, K. Kizior, P. Nowak, A. Karocki and B. Tokarczyk, *Phys. Chem. Chem. Phys.*, 2003, **5**, 988-997.

26 J. J. Chen, P. Zhao, H. B. Lv, Y. Yu and P. Y. Xu, *Chem. Commun.*, 2011, **47**, 2435; A. Picot, A. D'Aléo, P. L. Baldeck, A. Grichine, A. Duperray, C. Andraud and O. Maury, *J. Am. Chem. Soc.*, 2008, **130**, 1532; N. Rendón, A. Bourdolle, P. L. Baldeck, H. Le Bozec, C. Andraud, S. Brasselet, C. Coperet and O. Maury, *Chem. Mater.*, 2011, **23**, 3228.

27 F. Stellacci, C. A. Bauer, T. Meyer-Friedrichsen, W. Wenseleers, S. R. Marder and J. W. Perry, *J. Am. Chem. Soc.*, 2003, **125**, 328.

28 S. J. Yu, J. B. Chao, J. Sun, Y. G. Yin, J. F. Liu and G. B. Jiang, *Environ. Sci. Technol.*, 2013, **47**, 3268.

29 M. R. Gill, J. Garcia-Lara, S. J. Foster, C. Smythe, G. Battaglia and J. A. Thomas, *Nature Chem.*, 2009, **1**, 622.

30 M. Gao, C. K. Sim, C. W. T. Leung, Q. L. Hu, G. X. Feng, F. Xu, B. Z. Tang and B. Liu, *Chem. Commun.*, 2014, **50**, 8312; C. W. T. Leung, Y. Hong, S. Chen, E. Zhao, J. W. Y. Lam and B. Z. Tang, *J. Am. Chem. Soc.*, 2013, **135**, 62.

31 S. K. Manna, A. Mandal, S. K. Mondal, A. K. Adak, A. Jana, S. Das, S. Chattopadhyay, S. Roy, S. K. Ghorai, S. Samanta, M. Hossain and M. Baidya, *Org. Biomol. Chem.*, 2015, **13**, 8037.